Open Research Online

The Open University's repository of research publications
and other research outputs

Elemental abundances of blue compact dwarfs from mid-infrared spectroscopy with *Spitzer*

Journal Item

For guidance on citations see FAQs.

Version: Version of Record

Link(s) to article on publisher's website:
http://dx.doi.org/doi:10.1086/524005

oro.open.ac.uk

ELEMENTAL ABUNDANCES OF BLUE COMPACT DWARFS FROM MID-INFRARED SPECTROSCOPY WITH SPITZER

Yanling Wu,[1] J. Bernard-Salas,[1] V. Charmandaris,[2,3] V. Lebouteiller,[1]
Lei Hao,[1] B. R. Brandl,[4] and J. R. Houck[1]

ABSTRACT

We present a study of elemental abundances in a sample of 13 blue compact dwarf (BCD) galaxies, using the $\sim$10–37 μm high-resolution spectra obtained with Spitzer IRS. We derive the abundances of neon and sulfur for our sample using the infrared fine-structure lines probing regions which may be obscured by dust in the optical and compare our results with similar infrared studies of starburst galaxies from ISO. We find a good correlation between the neon and sulfur abundances, although sulfur is underabundant relative to neon with respect to the solar value. A comparison of the elemental abundances (neon and sulfur) measured from the infrared data with those derived from the optical (neon, sulfur, and oxygen) studies reveals a good overall agreement for sulfur, while the infrared-derived neon abundances are slightly higher than the optical values. This indicates either that the metallicities of dust-enshrouded regions in BCDs are similar to the optically accessible regions, or that if they are different they do not contribute substantially to the total infrared emission of the host galaxy.

Subject headings: dust, extinction — galaxies: starburst — nuclear reactions, nucleosynthesis, abundances

1. INTRODUCTION

Blue compact dwarf galaxies (BCDs) are dwarf galaxies with blue optical colors resulting from one or more intense bursts of star formation, low luminosities ($M_B > -18$), and small sizes. The first BCD discovered was I Zw 18 by Zwicky (1966), which had the lowest oxygen abundance observed in a galaxy (Searle & Sargent 1972) until the recent study of the western component of SBS 0335−052 (Izotov et al. 2005). Although BCDs are defined mostly by their morphological parameters, they are globally found to have low heavy-element abundances as measured from their H II regions ($1/30 \sim 1/2 \, Z_\odot$). The low metallicity of BCDs is suggestive of a young age, since their interstellar medium is chemically unevolved. However, some BCDs do display an older stellar population and have formed a large fraction of their stars more than 1 Gyr ago (see Loose & Thuan 1985; Aloisi et al. 2007). The plausible scenario that BCDs are young is intriguing within the context of cold dark matter models which predict that low-mass dwarf galaxies, originating from density perturbations much less massive than those producing the larger structures, can still be forming at the current epoch. However, despite the great success in detecting galaxies at high redshift over the past few years, bona fide young galaxies still remain extremely difficult to find in the local universe (Kunth & Sargent 1986; Kunth & Östlin 2000; Madden et al. 2006). This is likely due to the observational bias of sampling mostly luminous, more evolved galaxies at high redshifts. If some BCDs are truly young galaxies, they would provide an ideal local laboratory to understand the galaxy formation processes in the early universe.

Over the past two decades, BCDs have been studied extensively in many wavelengths using ground-based and space-borne instru-

ments (for a review, see Kunth & Östlin 2000). In the FUV, the *Far Ultraviolet Spectroscopic Explorer* (*FUSE*) has been used to study chemical abundances in the neutral gas in several BCDs (Thuan et al. 2002; Aloisi et al. 2003; Lebouteiller et al. 2004). Optical spectra have been obtained for a large number of BCDs and display strong narrow emission lines resulting from the intensive star formation processes that take place in these systems (Izotov et al. 1997; Izotov & Thuan 1999; Pustilnik et al. 2005; Salzer et al. 2005). The *Infrared Space Observatory* (*ISO*) unexpectedly revealed that despite their low metallicities, BCDs, such as SBS 0335−052E, could still have copious emission from dust grains (Thuan et al. 1999; Madden 2000; Madden et al. 2006; Plante & Sauvage 2002). More recently, the *Spitzer Space Telescope* (Werner et al. 2004) has been used to observe these metal-poor dwarf systems in order to study their dust continuum properties and polycyclic aromatic hydrocarbon (PAH) features (Houck et al. 2004b; Hogg et al. 2005; Engelbracht et al. 2005; Rosenberg et al. 2006; Wu et al. 2006, 2007; O'Halloran et al. 2006; Hunt et al. 2006). Finally, radio observations have also been performed for several BCDs to study their H I kinematics and distribution (Thuan et al. 2004) and thermal/nonthermal continuum emission properties (Hunt et al. 2005).

Metallicity is a key parameter that influences the formation and evolution of both stars and galaxies. Detailed studies of the elemental abundances of BCDs have already been carried out by several groups (Izotov & Thuan 1999; Kniazev et al. 2003; Shi et al. 2005), and the well-known metallicity-luminosity relation has also been studied in detail in the environment of dwarf galaxies (Skillman et al. 1989; Hunter & Hoffman 1999; Melbourne & Salzer 2002). However, because these studies were performed in the optical, they were limited by the fact that the properties of some of the deeply obscured regions in the star-forming galaxies may remain inaccessible due to dust extinction at these wavelengths. In fact, Thuan et al. (1999), using *ISO*, have shown that the eastern component of SBS 0335−052 does have an embedded super star cluster (SSC) that is invisible in the optical while contributing $\sim$75% to the bolometric luminosity (see also Plante & Sauvage 2002; Houck et al. 2004b), even though it has very low metallicity [$12 + \log (\text{O/H}) = 7.33$], which would in principle imply

[1] Astronomy Department, Cornell University, Ithaca, NY 14853; wyl@astro.cornell.edu, jbs@isc.astro.cornell.edu, vianney@isc.astro.cornell.edu, haol@astro.cornell.edu, jrh13@cornell.edu.

[2] Department of Physics, University of Crete, GR-71003 Heraklion, Greece; vassilis@physics.uoc.gr.

[3] IESL/Foundation for Research and Technology—Hellas, GR-71110 Heraklion, Greece; and Chercheur Associé, Observatoire de Paris, F-75014 Paris, France.

[4] Leiden Observatory, Leiden University, P.O. Box 9513, 2300 RA Leiden, The Netherlands; brandl@strw.leidenuniv.nl.

TABLE 1
OBSERVING PARAMETERS OF THE SAMPLE

| | | | | | | ON-SOURCE TIME (s) | |
| | R.A. | DECL. | | | | | |
OBJECT NAME	(J2000.0)	(J2000.0)	AORKEY	OBSERVATION DATE	REDSHIFT	SH	LR
Haro 11	00 36 52.5	−33 33 19	9007104	2004 Jul 17	0.0206	480	240
NGC 1140....................	02 54 33.6	−10 01 40	4830976	2004 Jan 7	0.0050	480	240
SBS 0335−052E.............	03 37 44.0	−05 02 40	11769856	2004 Sep 1	0.0135	1440	960
NGC 1569....................	04 30 47.0	+64 50 59	9001984	2004 Mar 1	∼0	480	240
II Zw 40......................	05 55 42.6	+03 23 32	9007616	2004 Mar 1	0.0026	480	240
UGC 4274....................	08 13 13.0	+45 59 39	12076032	2004 Oct 23	0.0015	120	56
			12626688	2004 Nov 11		120	56
I Zw 18	09 34 02.0	+55 14 28	9008640	2004 Mar 27	0.0025	480	240
			16205568	2005 Dec 16		2880	1440
VII Zw 403	11 27 59.9	+78 59 39	9005824	2004 Dec 9	∼0	480	240
Mrk 1450	11 38 35.6	+57 52 27	9011712	2004 Dec 12	0.0032	480	240
UM 461......................	11 51 33.3	−02 22 22	9006336	2005 Jan 3	0.0035	480	240
			16204032	2006 Jan 14		1440	...
SBS 1210+537A............	12 12 55.9	+53 27 38	8989952	2004 Jun 6	...	480	240
Tol 1214−277...............	12 17 17.1	−28 02 33	9008128	2004 Jun 28	0.0260	480	240
Tol 65........................	12 25 46.9	−36 14 01	4829696	2004 Jan 7	0.0090	480	240
UGC A292....................	12 38 40.0	+32 46 01	4831232	2004 Jan 7	0.0010	480	240
Tol 1304−353...............	13 07 37.5	−35 38 19	9006848	2004 Jun 25	0.0140	480	240
Pox 186......................	13 25 48.6	−11 37 38	9007360	2004 Jul 14	0.0039	480	240
CG 0563......................	14 52 05.7	+38 10 59	8992512	2005 May 30	0.0324	240	120
CG 0598......................	14 59 20.6	+42 16 10	8992256	2005 Mar 19	0.0575	480	240
CG 0752......................	15 31 21.3	+47 01 24	8991744	2005 Mar 19	0.0211	480	240
Mrk 1499	16 35 21.1	+52 12 53	9011456	2004 Jun 5	0.0090	480	240
[RC2]A2228−00	22 30 33.9	−00 07 35	9006080	2004 Jun 24	0.0052	480	240

NOTES.—The coordinates and redshifts of the objects are cited from the NASA/IPAC Extragalactic Database (NED). In this paper, we only include the analysis of 13 out of 22 sources which have S/Ns sufficient for our abundance study. CG 0563, CG 0598, and CG 0752 are included in the original sample as BCD candidates; however, they appear to be more starburst-like (see L. Hao et al. 2008, in preparation). Thus, even though they have high S/N, we do not include these three sources in this study. Units of right ascension are hours, minutes, and seconds, and units of declination are degrees, arcminutes, and arcseconds.

a low dust content. In addition to probing the dust-enshrouded regions, emission in the infrared also has the advantage that the lines accessible at these wavelengths are less sensitive to the electron temperature fluctuations than the corresponding optical lines of the same ion. In the infrared, more ionization stages of an element become available as well. The improved sensitivity of the Infrared Spectrograph (IRS;[5] Houck et al. 2004a) on *Spitzer* has enabled us to obtain for the first time infrared spectra for a much larger sample of BCDs than was previously possible (Thuan et al. 1999; Madden 2000; Verma et al. 2003; Martín-Hernández et al. 2006), thus motivating this study to probe the heavy-element abundances in BCDs.

In this paper we analyze *Spitzer* IRS spectra of 13 BCDs and present elemental abundances of neon and sulfur, which are both primary elements produced by the same massive stars in the nuclear synthesis processes. In § 2 we describe the sample selection, observations, and data reduction. We present our results on the chemical abundances in § 3, followed by a comparison of the optically and infrared-derived abundances in § 4. We show the interplay between the abundances and PAH emission in § 5. Finally, we summarize our conclusions in § 6.

2. OBSERVATIONS AND DATA REDUCTION

As part of the IRS Guaranteed Time Observation (GTO) program, we have compiled a large sample of BCD candidates selected from the Second Byurakan Survey (SBS), Bootes void galaxies (Kirshner et al. 1981; Popescu & Hopp 2000), and other commonly studied

BCDs. Details on the low-resolution spectra of the sample have been published by Wu et al. (2006).

We acquired the targets using the red (22 μm) IRS peak-up camera in high-accuracy mode to locate the mid-infrared centroid of the source and then offset to the appropriate slit using the standard IRS staring observing mode. Subsequently, we obtained the 10–37 μm spectra for our sources using the IRS Short-High (SH, 9.9–19.6 μm) and Long-High (LH, 18.7–37.2 μm) modules. No spectra of the background were obtained. The AORkey and on-source integration time of the 22 sources for which we obtain high-resolution spectroscopy are given in Table 1. In this paper we focus on the description and analysis of 13 BCDs from our program which have a signal-to-noise ratio (S/N) high enough for our elemental abundance study.

The data were processed by the *Spitzer* Science Center (SSC) pipeline version 13.2. The three-dimensional data cubes were converted to two-dimensional slope images after linearization correction, subtraction of darks, and cosmic-ray removal. The reduction of the spectral data started from intermediate pipeline products "droop" files, which only lacked stray light and flat-field correction. Individual pointings to each nod position of the slit were co-added. The data from SH and LH were extracted using the full-slit extraction method of a script version of the IRS data analysis package SMART (Higdon et al. 2004) from the median of the combined images. The one-dimensional spectra were flux calibrated by multiplying by a relative spectral response function (RSRF), which was created from the IRS standard star, ξ Dra, for which accurate templates were available (Cohen et al. 2003; G. Sloan et al. 2008, in preparation). As a final cosmetic step, the ends of each order where the noise increases significantly were manually clipped. No scaling was needed between the adjacent

TABLE 2
Optical Properties of the Sources

Object	$F(\mathrm{H}\beta)$ ($\times 10^{-14}$ ergs s^{-1} cm^{-2})				E_{B-V} (mag)	T_e (K)	N_e (cm^{-3})	Reference
	Huα-Derived	Hα-Derived	Radio-Derived	Optical				
Haro 11	252 ± 40	...	...	...	0.41	13,700	10	1
NGC 1140...........................	67 ± 9	...	...	...	0.10	10,000	100	2
SBS 0335−052E.................	<22.4	...	6.5 ± 0.06	...	2.76	20,000	200	3, 4, 5
NGC 1569...........................	393 ± 19	...	...	...	0.65	12,000	100	6
II Zw 40..............................	363 ± 10	282 ± 22	...	...	0.79	13,000	190	2, 7
UGC 4274...........................	<59.6	11.5 ± 1.0	...	...	0	10,000	62	7, 8
I Zw 18	<12.6	8.0 ± 0.6	6.1 ± 0.6	...	0.08	19,000	100	7, 9, 10
VII Zw 403	<24.6	11.8 ± 1.2	...	...	0	14,800	100	7, 11
Mrk 1450	<14.8	15.8 ± 1.4	...	...	0.10	12,500	100	7, 12
UM 461...............................	<21.0	...	...	13.6 ± 0.6	0.08	16,100	200	13, 14
Tol 1214−277......................	23.3 ± 2.8	...	...	...	0.03	19,790	400	15
Tol 65.................................	<18.2	9.3 ± 0.4	...	...	0.08	17,320	50	7, 15
Mrk 1499	14.6 ± 1.9	15.1 ± 1.3	...	...	0.17	12,600	3267	7, 16

Notes.—When no data are available in the literature, the electron temperature and densities are assumed to be 10,000 K (for NGC 1140 and UGC 4274) and 100 cm^{-3} (for NGC 1140 and NGC 1569), respectively. When the Huα line is detected, the Hβ flux is preferentially derived from this line. The upper limits are listed for the non-detections. For the remaining sources, we derived the Hβ flux either from the thermal component of the radio continuum or from the extinction-corrected Hα flux inside the SH slit. For UM461, the Hβ flux is for the whole galaxy from the integrated optical spectra.

References.—(1) Bergvall & Oumlstlin 2002; (2) Guseva et al. 2000; (3) Izotov et al. 2006; (4) Hunt et al. 2004; (5) Houck et al. 2004b; (6) Kobulnicky & Skillman 1997; (7) Gil de Paz et al. 2003; (8) Ho et al. 1997; (9) Cannon et al. 2005; (10) Izotov et al. 1999; (11) Izotov et al. 1997; (12) Izotov et al. 1994; (13) Moustakas & Kennicutt 2006; (14) Izotov & Thuan 1998; (15) Izotov et al. 2001; (16) Kong et al. 2002.

orders within the same module. For faint sources, the spectra taken at nod position 1 are severely affected by fringing problems; thus, we only use the data at nod position 2 for these sources in our study.

The fine-structure lines, [S IV] $\lambda 10.51$ μm, [Ne II] $\lambda 12.81$ μm, [Ne III] $\lambda 15.55$ μm, and [S III] $\lambda\lambda 18.71$, 33.48 μm, are clearly present in the majority of the BCDs in our sample.[6] We measure the line fluxes by fitting them with a Gaussian profile. Even though the [S III] line is visible in both SH and LH, we only use the 18.71 μm line for deriving the ionic abundance. This is because by using lines within the same module (SH), we remove uncertainties due to the different sizes of the SH and LH slits. Furthermore, the [S III] $\lambda 33.48$ μm line is near the cut-off of the LH module where the sensitivity drops dramatically, making its measurement more uncertain in some cases.

3. ELEMENTAL ABUNDANCES OF BCDs

In this section, we derive the neon and sulfur abundances using the new infrared data of our BCD sample. The elemental abundances of the compact H II regions in our Galaxy (Martín-Hernández et al. 2002; Simpson et al. 2004), in the Magellanic Clouds (Vermeij & van der Hulst 2002), and in starburst galaxies (Verma et al. 2003; Martín-Hernández et al. 2006) have already been studied extensively in the past using *ISO*, and more recently with *Spitzer* (Rubin et al. 2007). There are several methods to derive the chemical abundances (for a review, see Stasińska 2007). Here we use an empirical method, which derives ionic abundances directly from the observed lines of the relevent ions. To do so, we need to have the flux of at least one hydrogen recombination line and the dust extinction, as well as the electron temperature and density of the interstellar medium (ISM).

3.1. *Electron Density and Temperature*

The electron density (N_e) could in principle be determined by comparing the measured ratio of [S III] 18.71/33.48 μm to the expected theoretical value using the corresponding S-curve (see

Houck et al. 1984). However, the values of this ratio for the BCD sample are in the horizontal part of the S-curve, and as a result we cannot use these two lines to accurately constrain the electron density of these systems. Furthermore, the 33.48 μm [S III] line is located at the edge of the LH slit, where the sensitivity drops dramatically, and considering that these emission lines are weak, the measured line flux for the 33.48 μm [S III] line has a large uncertainty. Since the infrared determination of elemental abundances does not depend strongly on the density, we adopted optically derived electron densities from the literature, which range from 10 to 3000 cm^{-3} (see Table 2). For sources where such information is not available, we adopt a typical electron density of 100 cm^{-3} in this paper.

Since BCDs in general have low metallicities, it is expected that BCDs would have relatively high electron temperatures (T_e). Fortunately, the infrared lines are much less sensitive to the uncertainties in the electron temperature compared to the optical (Bernard-Salas et al. 2001). As a result, we adopt electron temperatures derived from the optical studies found in the literature. For sources which do not have direct measurements (which happen to be high-metallicity sources in our sample, e.g., NGC 1140 and UGC 4274), we use a representative temperature of $T_e = 10,000$ K (see Table 2).

3.2. *Ionized Hydrogen Flux Estimates*

In order to derive the ionic abundances, we also need to obtain information on at least one hydrogen recombination line (usually Hβ). For sources in which the Humphreys α (Huα, 12.37 μm) line is detected, we use it to convert to Hβ. From the extinction-corrected Huα flux, we estimate the Hβ flux using the values given in the tables of Hummer & Storey (1987) for Case B recombination. This has the advantage that we do not need to correct for aperture effects because the neon and sulfur lines we use to derive the abundances also reside in the same module (SH). The 12.37 μm line is generally very weak, and it is detected in six of our 13 sources. For SBS 0335−052E and I Zw 18, which have radio continuum data, we calculate the Hβ flux from the thermal free-free emission using the fraction included in the aperture of

---
[6] See Fig. 3 of Wu et al. (2006) or L. Hao et al. (2008, in preparation) for the reduced spectra.

TABLE 3
FINE-STRUCTURE LINE FLUXES AND IONIC ABUNDANCES

	LINE FLUXES ($\times 10^{-14}$ ergs cm^{-2} s^{-1})				IONIC ABUNDANCES ($\times 10^{-6}$)			
OBJECT	[S IV] (10.51 μm)	[Ne II] (12.81 μm)	[Ne III] (15.55 μm)	[S III] (18.71 μm)	$N_{\text{S IV}}/N_p$	$N_{\text{Ne II}}/N_p$	$N_{\text{Ne III}}/N_p$	$N_{\text{S III}}/N_p$
Haro 11	43.95 ± 0.14	31.23 ± 0.23	98.14 ± 0.65	45.24 ± 0.25	0.353 ± 0.056	15.4 ± 2.4	23.2 ± 3.7	1.89 ± 0.30
NGC 1140	12.14 ± 0.13	11.41 ± 0.20	37.79 ± 0.32	20.04 ± 0.11	0.375 ± 0.051	22.5 ± 3.0	35.5 ± 4.8	3.56 ± 0.48
SBS 0335−052E	1.56 ± 0.03	<0.14	1.43 ± 0.02	0.43 ± 0.03	0.527 ± 0.011	<2.27	11.2 ± 1.6	0.535 ± 0.038
NGC 1569	147.26 ± 0.55	15.70 ± 0.17	175.85 ± 0.59	72.70 ± 0.23	0.817 ± 0.040	5.28 ± 0.26	28.2 ± 1.4	2.12 ± 0.10
II Zw 40	185.72 ± 1.73	6.24 ± 0.11	112.65 ± 0.83	45.80 ± 0.21	1.12 ± 0.03	2.23 ± 0.07	19.3 ± 0.6	1.37 ± 0.04
UGC 4274	4.18 ± 0.12	8.87 ± 0.11	12.84 ± 0.12	12.63 ± 0.11	0.743 ± 0.068	102 ± 9	70.3 ± 6.1	13.2 ± 1.2
I Zw 18	0.48 ± 0.03	0.09 ± 0.01	0.46 ± 0.02	0.23 ± 0.02	0.125 ± 0.015	1.41 ± 0.21	3.56 ± 0.38	0.276 ± 0.036
VII Zw 403	0.99 ± 0.05	<0.142	0.88 ± 0.02	0.87 ± 0.02	0.311 ± 0.035	<2.79	8.41 ± 0.88	1.39 ± 0.14
Mrk 1450	7.34 ± 0.04	1.34 ± 0.03	9.61 ± 0.04	4.37 ± 0.03	0.928 ± 0.223	10.70 ± 2.57	36.9 ± 8.9	2.98 ± 0.71
UM 461	4.58 ± 0.04	0.16 ± 0.02	2.83 ± 0.03	0.812 ± 0.03	0.636 ± 0.029	1.38 ± 0.18	11.8 ± 0.5	0.563 ± 0.032
Tol 1214−277	0.88 ± 0.02	<0.10	0.61 ± 0.02	<0.19	0.061 ± 0.007	<0.413	1.23 ± 0.15	<0.059
Tol 65	0.69 ± 0.02	<0.14	0.90 ± 0.02	0.32 ± 0.02	0.129 ± 0.007	<1.62	5.07 ± 0.25	0.293 ± 0.022
Mrk 1499	1.74 ± 0.02	1.88 ± 0.03	5.03 ± 0.03	2.91 ± 0.02	0.286 ± 0.037	16.5 ± 2.2	21.6 ± 2.8	2.28 ± 0.30

NOTES.—The observed line fluxes are measured from the IRS high-resolution spectra of the sources. Background emission has not been subtracted, but this does not affect the flux of the fine-structure lines.

our SH slit at the time of the observation, and no correction for extinction is needed. For the remaining four sources which have Hα images available from Gil de Paz et al. (2003), we overlay the SH slit on each Hα image to calculate what fraction of the Hα emission is included in our slit. Then we derive the corresponding Hβ flux inside the SH slit from the extinction-corrected Hα flux. Finally, for UM 461, we use the Hβ flux of the whole galaxy from the integrated spectra (Moustakas & Kennicutt 2006). UM 461 is a very compact source, and thus is fully encompassed within the SH slit.

3.3. Extinction Correction

All our measurements, both the fluxes from the Hα images and the infrared lines, have been corrected for extinction. From the low-resolution spectra of our BCDs (Wu et al. 2006), we find that most of the sources do not show a strong 9.7 μm silicate feature, thus indicating an intrinsically relatively low dust extinction. Due to the faintness of our targets at $\lambda < 9.7$ μm, the determination of the continuum on the blue side of the 9.7 μm feature is often poor, and the uncertainties in estimating the mid-infrared extinction from this are rather large (see discussion in Spoon et al. 2007). Thus, for sources where optical spectra are available, we adopt the E_{B-V} values calculated from the hydrogen recombination lines in the literature. Only for SBS 0335−052E, which has a high quality mid-infrared spectrum and evidence for an embedded SSC, the optical E_{B-V} is not a good estimate of its extinction, thus we use the extinction estimated from the depth of the silicate feature (Houck et al. 2004b). Throughout this paper, we adopt the Fluks et al. (1994) extinction law, although using the Draine (2003) law would produce very similar results. The E_{B-V} magnitudes are provided in Table 2.

3.4. Neon and Sulfur Abundances Determination

We use the electron density and temperature given in Table 2, together with the fine structure lines detected in the IRS high-resolution spectra, to calculate the abundances of neon and sulfur. The equation used to determine the ionic abundance is described in Bernard-Salas et al. (2001) and is

$$\frac{N_{\text{ion}}}{N_p} = \frac{I_{\text{ion}}}{I_{\text{H}\beta}} N_e \frac{\lambda_{\text{ul}}}{\lambda_{\text{H}\beta}} \frac{\alpha_{\text{H}\beta}}{A_{\text{ul}}} \left(\frac{N_u}{N_{\text{ion}}}\right)^{-1}, \qquad (1)$$

where $I_{\text{ion}}/I_{\text{H}\beta}$ is the measured flux of the fine-structure line normalized to Hβ, N_p is the density of the ionized hydrogen, λ_{ul} and $\lambda_{\text{H}\beta}$ are the wavelengths of the line and Hβ, $\alpha_{\text{H}\beta}$ is the effective recombination coefficient for Hβ, A_{ul} is the Einstein spontaneous transition rate for the line, and N_u/N_{ion} is the ratio of the population of the level from which the line originates to the total population of the ion. This ratio is determined by solving the statistical equilibrium equation for a five-level system and normalizing the total number of ions to be unity (Osterbrock 1989). The effective collisional strengths used to derive the population of levels were obtained from the appropriate reference of the IRON project (Hummer et al. 1993).[7]

The most important ionization stages of neon and sulfur are available in the infrared. We detected [S IV] $\lambda 10.51$ μm and [Ne III] $\lambda 15.56$ μm in all of our BCDs, while the [Ne II] $\lambda 12.81$ μm line is detected in nine objects and [S III] $\lambda 18.71$ μm in 12 sources (see Table 3). For sulfur, S II has its strongest emission lines in the optical. Vermeij & van der Hulst (2002) have shown that S II is typically less than 10% of S III in the Magellanic Cloud H II regions they studied. Because BCDs are typically high-excitation objects, we do not expect to have a significant contribution from S II. The optical studies reveal that the ionic abundance of S II is typically 10%–20% of that of S III (Izotov et al. 1994, 1997); thus, we keep in mind that this might result in a ∼10% underestimate in our infrared derived sulfur abundance. This is addressed further in the following subsection, where we discuss the properties of the individual objects. The presence of the [O IV] $\lambda 25.89$ μm line in most of our sources (except for VII Zw 403, UM 461, Tol 65, and Mrk 1499) indicates that some [Ne IV] might be present, even though the [O IV] line is typically weak. For example, in Tol 1214−277, where [O IV] is detected, the flux of [Ne IV]$\lambda 4725$ from optical spectra is less than 1% of that of [Ne III] $\lambda 3868$ (Izotov et al. 2004), indicating that the contribution of [Ne IV] is not significant. Tsamis & Péquignot (2005) also have shown in their photoionization modeling study of 30 Doradus that the contribution from Ne IV to the total neon abundance is much less than 1%. As a result, rather than applying ionization correction factors (ICFs) which could introduce an unknown systematic uncertainty in our study, we sum the corresponding ionic abundances for the most
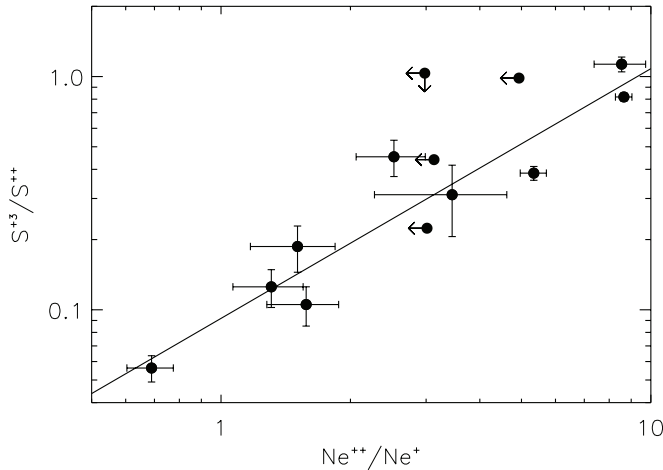
---

[7] See http://www.usm.uni-muenchen.de/people/ip/iron-project.html.

Fig. 1.—Ne^{++}/Ne$^+$ vs. S^{+3}/S^{++}, tracing the hardness of the radiation field. The solid line is a fit to the data.

important ionization stages to determine the total element abundance, and the results are shown in Table 3.

Two successive stages of ionization of a given element (X) can be used to measure the state of the ionization of the ISM, which, on first order, depends on the ionization parameter, U, and the hardness of the ionizing radiation (Vilchez & Pagel 1988). For a given U, the ratio X^{+i+1}/X^{+i} is an indicator of the hardness of the stellar radiation field. Here we use the ionic pairs of Ne^{++}/Ne$^+$ and S^{+3}/S^{++} as indicators of the hardness of the ionization field and plot them in Figure 1. It is clear from the figure that these two ratios increase proportionally. This indicates that the hardening of the radiation field affects similarly the various elements in the full range of the ionizing continua.

The major uncertainty in our study of the elemental abundances originates from the Hβ fluxes used as references. For sources in which the 12.37 μm Huα line is detected, we have no uncertainties from matching the slit apertures, and the extinction correction is very small. For sources where we estimate the Hβ flux from the thermal radio continuum emission, we are free of extinction corrections, even though we still need to properly account for the radio emission which falls within the IRS slit. For BCDs with no Huα emission or radio data available in the literature, we estimate the Hβ flux using archival Hα images of the objects. This is clearly more challenging, because in addition to the aperture corrections, the extinction correction is higher, which could introduce a systematic uncertainty as large as 25%. In the following analysis, we indicate the sources with or without the detection of the Huα line using different symbols on the plots (see Figs. 2, 3, and 4). The measurement uncertainties in the infrared lines are typically only a few percent, but could grow to ~10% in the case of fainter sources. The uncertainties we list in Table 3 only account for measurement uncertainties.

3.5. *Individual Objects*

Some details on the individual objects and how we measured the necessary parameters are provided in the following paragraphs.

Haro 11.—The 12.37 μm Huα line is clearly detected in the SH spectrum. The source has multiple nuclei, designated as A, B, and C (Bergvall & Oumlstlin 2002). The optical spectra from which the oxygen abundance was derived correspond to the central region. Because all the lines we are using are from the SH spectrum, we are relatively free from extinction problems and there is no need for aperture correction. The contribution of S II may add ~10% to the total sulfur abundance.

NGC 1140.—As with Haro 11, the 12.37 μm Huα line is clearly detected in the SH spectrum of NGC 1140. No measurement was found in the literature for the electron temperature or density for this source, thus we assume 10,000 K and 100 cm^{-3}, respectively, which are typical for BCDs. However, because its oxygen abundance is more than half solar, the electron temperature could also be lower. If we use a T_e of 5000 K and rederive the abundances, we find that the neon abundance would increase from 5.8×10^{-5} to 8.5×10^{-5} and the sulfur abundance from 3.9×10^{-6} to 5.5×10^{-6}. The contribution of S II may add ~10% to the total sulfur abundance.

SBS 0335$-$052E.—We do not detect the 12.37 μm Huα line in the SH spectrum. We use the thermal component of the 5 GHz radio continuum from Hunt et al. (2004) to convert to the Hβ flux, and thus no extinction correction is needed. [Ne II] is not detected, and we provide the upper limit in Table 3. The ionic abundance of S II is ~25% of the S III determined from the optical study of Izotov et al. (2006) and may add 12% to the total sulfur abundance. We also find higher neon and sulfur abundances compared with oxygen, and possible implications are discussed in Houck et al. (2004b).

NGC 1569.—The 12.37 μm Huα line is clearly detected in the SH spectrum, thus providing a direct estimate of the Hβ flux inside the SH slit. This galaxy is extended in the mid-infrared (see Fig. 4 in Wu et al. 2006), and optical spectra have been taken for several of the bright knots by Kobulnicky & Skillman (1997) in order to study the chemical gradient and inhomogeneities of the source. These authors found very little variation in the metallicity. Our infrared-derived abundances are in rough agreement with the optical results. The ionic abundance of S II is ~13% that of the S III estimated from the optical study (Kobulnicky & Skillman 1997) and may add 9% to the total sulfur abundance.

II Zw 40.—We use the 12.37 μm Huα line to convert to Hβ flux. The derived neon and sulfur abundances agree with each other but appear to be lower than oxygen with respect to the solar values. If we estimate the Hβ flux from the Hα image of Gil de Paz et al. (2003) we find a value ~22% lower than the first, which would increase the neon and sulfur abundances by 22% accordingly. This suggests that when using the Hβ flux derived from Hα image, the systematic error in our measurement is probably no better than 25%. The ionic abundance of S II is ~13% that of S III from the optical study of Guseva et al. (2000) and may add 7% to the total sulfur abundance.

UGC 4274.—We use an Hβ flux derived from the Hα image of Gil de Paz et al. (2003). Similarly to NGC 1569, the galaxy is extended and the peak of the infrared centroid is displaced from the optical peak position. The derived neon and sulfur abundances are both supersolar. The oxygen abundance is not directly available from the literature, thus we use the [N II]/Hα method (Ho et al. 1997; Denicoló et al. 2002) to derive O/H, which bears a large uncertainty. The contribution of S II may add ~10% to the total sulfur abundance.

I Zw 18.—The Hβ flux is derived from the thermal component of the radio continuum inside the SH slit. The ionic abundance of S II is ~21% that of S III from the optical study of Izotov et al. (1999) and may add 15% to the total sulfur abundance. A more detailed discussion on this object can be found in Wu et al. (2007).

VII Zw 403.—The Hβ flux is derived by using the Hα image from Gil de Paz et al. (2003). The optical and infrared centroids do not overlap. The SH spectrum for this source is noisy and [Ne II] λ12.81 μm is not detected; thus, we have only a lower limit on the neon abundance. The upper limit of the [Ne II] line indicates that it could add less than 25% to the total elemental abundance of neon which is presented in Table 4. The ionic abundance

TABLE 4
Elemental Abundances

Object	Ne/H ($\times 10^{-6}$)	S/H ($\times 10^{-6}$)	O/H ($\times 10^{-5}$)	Ne ($Z_\odot$)	S ($Z_\odot$)	O ($Z_\odot$)	References (O/H)
Haro 11	38.6 ± 4.4	2.24 ± 0.31	7.94	0.33 ± 0.04	0.16 ± 0.02	0.16	1
NGC 1140	58.0 ± 5.7	3.94 ± 0.48	28.8	0.48 ± 0.05	0.28 ± 0.03	0.59	2
SBS 0335−052E..............	$[11.2, 13.5]^a$	1.06 ± 0.04	1.95 ± 0.09	$[0.09, 0.11]^a$	0.08 ± 0.003	0.03 ± 0.001	3
NGC 1569.........................	33.5 ± 1.4	2.94 ± 0.11	15.8 ± 0.5	0.28 ± 0.01	0.21 ± 0.01	0.32 ± 0.01	4
II Zw 40	21.5 ± 0.6	2.49 ± 0.05	12.2 ± 0.4	0.17 ± 0.005	0.18 ± 0.004	0.25 ± 0.01	2
UGC 4274.........................	172.3 ± 10.9	13.94 ± 1.20	33.3	1.4 ± 0.1	1.0 ± 0.1	0.68	5
I Zw 18	5.0 ± 0.4	0.40 ± 0.04	1.47 ± 0.09	0.04 ± 0.003	0.03 ± 0.003	0.03 ± 0.002	6
VII Zw 403	$[8.4, 11.2]^a$	1.70 ± 0.14	4.90 ± 0.11	$[0.07, 0.09]^a$	0.12 ± 0.01	0.10 ± 0.002	7
Mrk 1450	47.6 ± 9.2	3.98 ± 0.74	9.55 ± 0.11	0.40 ± 0.08	0.28 ± 0.06	0.19 ± 0.002	8
UM 461............................	13.2 ± 0.5	1.20 ± 0.04	6.10 ± 0.40	0.11 ± 0.01	0.09 ± 0.003	0.12 ± 0.01	9
Tol 1214−277...................	$[1.2, 1.6]^a$	$[0.06, 0.12]^b$	3.45 ± 0.10	$[0.010, 0.013]^a$	$[0.004, 0.008]^b$	0.07 ± 0.002	10
Tol 65..............................	$[5.1, 6.7]^a$	0.42 ± 0.07	3.48 ± 0.10	$[0.04, 0.06]^a$	0.03 ± 0.002	0.07 ± 0.02	10
Mrk 1499	38.1 ± 3.6	2.57 ± 0.30	13.2	0.32 ± 0.03	0.18 ± 0.02	0.27	11

Note.—We adopt the following values for the solar abundances: $(Ne/H)_\odot = 1.2 \times 10^{-4}$, $(S/H)_\odot = 1.4 \times 10^{-5}$, and $(O/H)_\odot = 4.6 \times 10^{-4}$ (see § 4.1).

[a] We provide a range for the neon abundance by taking as the lower value the ionic abundance of Ne III, while to obtain the upper value we add the upper limit for Ne II.

[b] We provide a range for the sulfur by taking as the lower value the ionic abundance of S IV, while to obtain the upper value we add the upper limit of S III.

References.—(1) Bergvall & Oumlstlin 2002; (2) Guseva et al. 2000; (3) Izotov et al. 2006; (4) Kobulnicky & Skillman 1997; (5) Ho et al. 1997; (6) Izotov et al. 1999; (7) Izotov et al. 1997; (8) Izotov et al. 1994; (9) Izotov & Thuan 1998; (10) Izotov et al. 2001; (11) Kong et al. 2002.

of S II is ∼24% that of S III from the optical work of Izotov et al. (1997) and may add 20% to the total sulfur abundance.

Mrk 1450.—As with VII Zw 403, we use the hydrogen flux as given by the Hα flux included in the SH slit. Neon and sulfur abundances appear to be higher than the oxygen abundance with respect to the solar values. The ionic abundance of S II is ∼18% that of S III from the optical study of Izotov et al. (1994) and may add 12% to the total sulfur abundance.

UM 461.—The Hβ flux is estimated from the integrated spectra of Moustakas & Kennicutt (2006), and the source is small enough to be fully included by the SH slit. The derived neon and sulfur abundances are in good agreement with oxygen metallicity from the optical. The ionic abundance of S II is ∼17% that of S III from the optical (Izotov & Thuan 1998) and may add 8% to the total sulfur abundance.

Tol 1214−277.—The 12.37 μm Huα line is marginally detected in the SH spectrum, and we use this line to derive the Hβ flux. The spectrum is very noisy, and no [Ne II] λ12.81 μm or [S III] λ18.71 μm lines are visible. We use the ionic abundances of [Ne III] and [S IV] as the lower limits of the neon and sulfur abundances. The upper limit of [Ne II] amounts to 33% of the ionic abundance of [Ne III], while the upper limit of [S III] is nearly as much as the abundance of [S IV]. We give the range of their elemental abundances in Table 4. The ionic abundance of S II is ∼18% that of S III from the optical study of Izotov et al. (2001) and may add ∼9% to the total sulfur abundance.

Tol 65.—We use the Hα image (Gil de Paz et al. 2003) to calculate the Hβ flux. [Ne II] λ12.81 μm is not detected in the SH spectrum; thus, our derived neon abundance is a lower limit. The upper limit of Ne II is ∼32% of the ionic abundance of Ne III, and the range of neon abundance is provided in Table 4. The metallicity of sulfur relative to solar is lower than oxygen. The ionic abundance of S II is ∼26% that of S III from the optical (Izotov et al. 2001) and may add 19% to the total sulfur abundance.

Mrk 1499.—The 12.37 μm Huα line is detected in the SH spectrum. There was a bad pixel at the peak of this line and we interpolated its value using adjacent pixel values. The infrared centroid appears to be slightly shifted from the optical one. The Hβ flux inside the SH slit derived from the Hα image is very similar to

that derived from the Huα line (within ∼10%). The contribution of S II may add ∼10% to the total sulfur abundance.

4. DISCUSSION

In this section we compare the abundances derived from the infrared spectra with the results from the optical studies.

4.1. Solar Abundances

The solar photospheric abundances have changed drastically over the past few years (see discussion in Pottasch & Bernard-Salas 2006). In some cases, the solar abundance estimates for the same element from different authors could differ by a factor of 2. In this paper, when we quote the elemental abundance in solar units (e.g., Table 4), we adopt the following values: $(Ne/H)_\odot = 1.2 \times 10^{-4}$ from Feldman & Widing (2003), $(S/H)_\odot = 1.4 \times 10^{-5}$ from Asplund et al. (2005), and $(O/H)_\odot = 4.9 \times 10^{-4}$ from Allende Prieto et al. (2001). We should note, however, that Asplund et al. (2005) have also reported that $(Ne/H)_\odot = 6.9 \times 10^{-5}$, and Grevesse & Sauval (1998) have given $(S/H)_\odot = 2.1 \times 10^{-5}$, while Anders & Grevesse (1989) have reported that $(O/H)_\odot = 8.5 \times 10^{-4}$. These values represent the extremes for the solar neon, sulfur, and oxygen abundance determinations. Pottasch & Bernard-Salas (2006) have shown that the higher neon solar value is favored in their sample of planetary nebulae (PNe). In the present paper we indicate the range of solar abundances in our plots, and we also discuss the impact of different solar values on our results.

4.2. Neon and Sulfur Abundances

As discussed in Thuan et al. (1995), it is assumed—and has been shown in the optical—that the α-element–to–oxygen abundance ratios do not vary with oxygen abundance. This is due to the fact that those elements are produced by the same massive stars ($M > 10 \, M_\odot$) responsible for oxygen production. We test this assumption in the infrared by studying the abundances of neon and sulfur as derived from our IRS data.

In Figure 2 we plot the abundances of neon and sulfur as derived from our high-resolution data. Verma et al. (2003) have found a positive correlation between the neon and argon abundances for their sample of starburst galaxies, while their data show
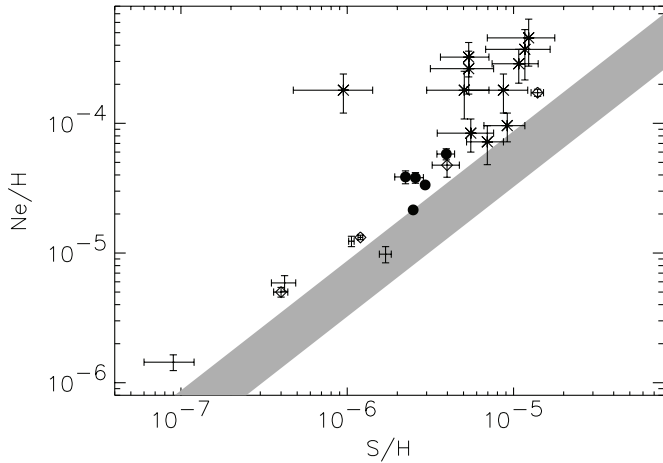
Fig. 2.—Ne/H vs. S/H abundance. Our BCDs are indicated by filled circles if Huα is detected and by diamonds if it is not detected. The sources that are shown by only the error bars are those that have a nondetection of [Ne II] or [S III] (see the note to Table 4). The starburst galaxies from Verma et al. (2003) are marked with stars. We use the gray band to indicate the locus on the plot where the ratio of Ne/S would be consistent with the different solar values for neon and sulfur abundances.

Fig. 3.—Abundance ratio of Ne/S as a function of Ne/H. The symbols are the same as in Fig. 1. The gray area indicates the range for the values of the Ne/S ratio encountered in the solar neighborhood.

no correlation between the sulfur and neon and/or argon abundances (indicated as stars on Fig. 2). However, our sources show that the neon and sulfur abundances scale with each other. In the same figure, we also plot the proportionality line of the ratio for $(Ne/S)_\odot$. The maximum and minimum values of the solar neon and sulfur abundances are indicated by the width of the gray band, and we find that most of our BCDs have ratios above those values.

In Figure 3 we examine the ratio of Ne/S[8] as a function of Ne/H derived from the IRS data. We see no correlation between the ratio of Ne/S with respect to Ne/H, in agreement with the results of Thuan et al. (1995). The average Ne/S ratio we found for these BCDs is 12.5 ± 3.1. This is similar to the Ne/S ratio of 14.3 in the Orion Nebula (Simpson et al. 2004). The Ne/S ratios found in the H II regions of M83 are higher (∼24–42) and decrease with increasing deprojected galactocentric radii (Rubin et al. 2007). These authors have also found that the Ne/S ratios in M33 are ∼12–21 (Rubin et al. 2006). We notice that all the BCDs, as well as the H II regions in M33, M83, and the Orion Nebula, have larger Ne/S ratios than those found in the solar neighborhood, while their Ne/S ratios from optical measurements are more consistent with the solar ratios. The higher Ne/S ratios from infrared studies have already been found in other types of object, including PNe, starburst galaxies, and other H II regions (Marigo et al. 2003; Verma et al. 2003; Henry et al. 2004; Pottasch & Bernard-Salas 2006). Some of these works point out that the solar sulfur abundance could have been underestimated and they also appear to favor the higher values for the solar neon abundance. It could also be due to a differential depletion of sulfur onto dust grains compared to neon as suggested by several studies (Simpson & Rubin 1990; Verma et al. 2003; Pottasch & Bernard-Salas 2006; Bernard-Salas et al. 2008).

4.3. Comparison with Optically Derived Abundances

As has been discussed earlier in this paper, one of the major advantages of using infrared lines for estimating abundances is that one can probe emission from dust-enshrouded regions without the uncertainties introduced from extinction corrections. In

this subsection, we compare the newly derived neon and sulfur abundances of our BCD sample using the infrared data, with the abundances of the same elements as well as those for oxygen estimated from optical studies available in the literature.

In order to determine elemental abundances, the optical studies usually adopt a two-zone photoionized H II region model: a high-ionization zone with temperature $T_e(O\ III)$ and a low-ionization zone with temperature $T_e(O\ II)$. Because the infrared lines are much less sensitive to variations in T_e (which affect the calculation of the population of the various atomic levels), in the subsequent calculations we assume a constant electron temperature for our analysis.

In Figure 4 we compare the infrared derived neon and sulfur abundances of the BCD sample with their optical metallicities, using the oxygen abundances from the literature (see also Table 4). The infrared neon abundances with respect to solar are slightly higher than that for oxygen (see Fig. 4a), but overall, there is a good agreement between the infrared measurements and the optical results. This indicates that there is little dust-enshrouded gas, or that these regions have similar metallicities, or that they do not contribute much to the total integrated emission of the galaxies. In SBS 0335−052E, as well as Mrk 1450, UGC 4274, and Haro 11, the infrared-derived metallicity of neon is more than twice that of oxygen compared to the solar values. This could be due to the different regions we are probing using the infrared, which could be obscured in the optical. SBS 0335−052E is known to have an embedded super star cluster that is invisible in the optical (see Houck et al. 2004b). Both Haro 11 and UGC 4274 are somewhat extended, and detailed spectroscopy over the whole galaxy would be needed to directly compare the infrared results with the optical ones. For Mrk 1450, which is a point source for *Spitzer* IRS, the abundance we derived using the infrared data is higher than the optical value and it is likely due to the fact that the optical estimates are more susceptible to the uncertainties in the electron temperature. If we lower T_e from 12,500 to 10,000 K, the oxygen abundance calculated from the optical data would double, while the neon abundance measured from the infrared would only increase by 5%. In Figure 4b we show that the infrared-derived sulfur abundances agree well with the oxygen abundance relative to solar.

For 9 out of the 13 objects we studied, optically derived neon and sulfur abundances are also available in the literature. The optical data have matched apertures, in most cases an accurate T_e

---

[8] For sources for which abundances are shown as a range, i.e., $[x, y]$, in Table 4, we assume the average of $(x + y)/2$ as their abundance when calculating the Ne/S ratios.
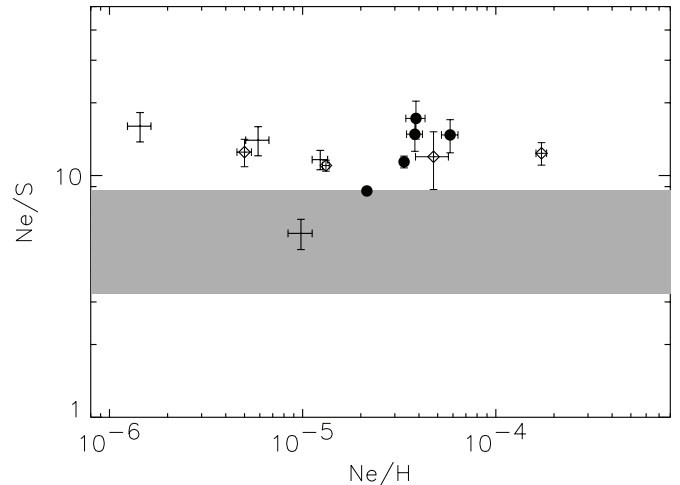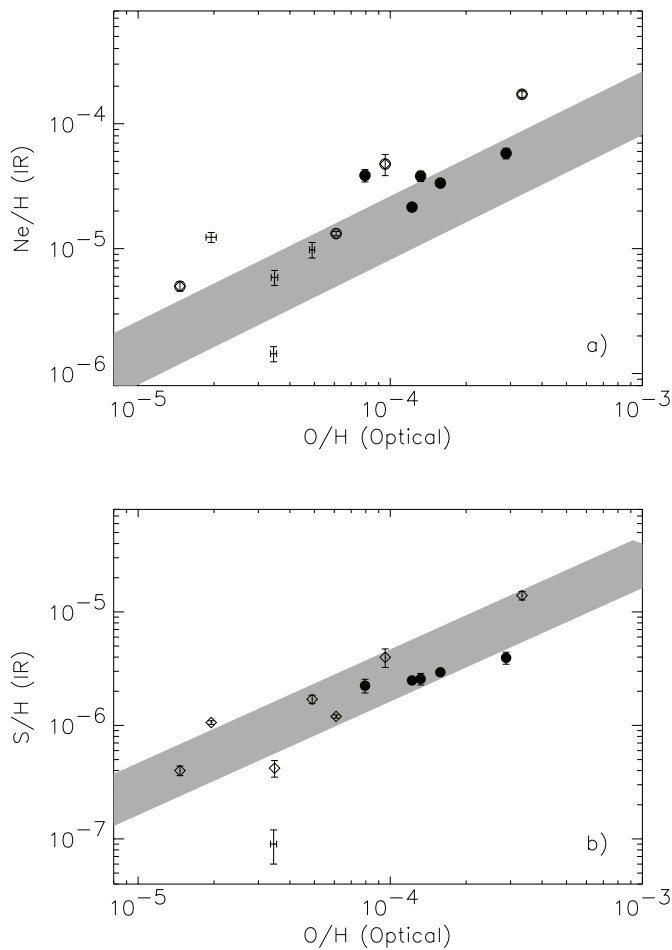
Fig. 4.—(a) Ne/H vs. O/H abundances. The symbols are the same as in Fig. 1. The gray band represents the locus on the plot where sources of different metallicities would have a Ne/O intrinsic ratio similar to the values found in the solar neighborhood. (b) Same as (a), but for S/H vs. O/H abundances.
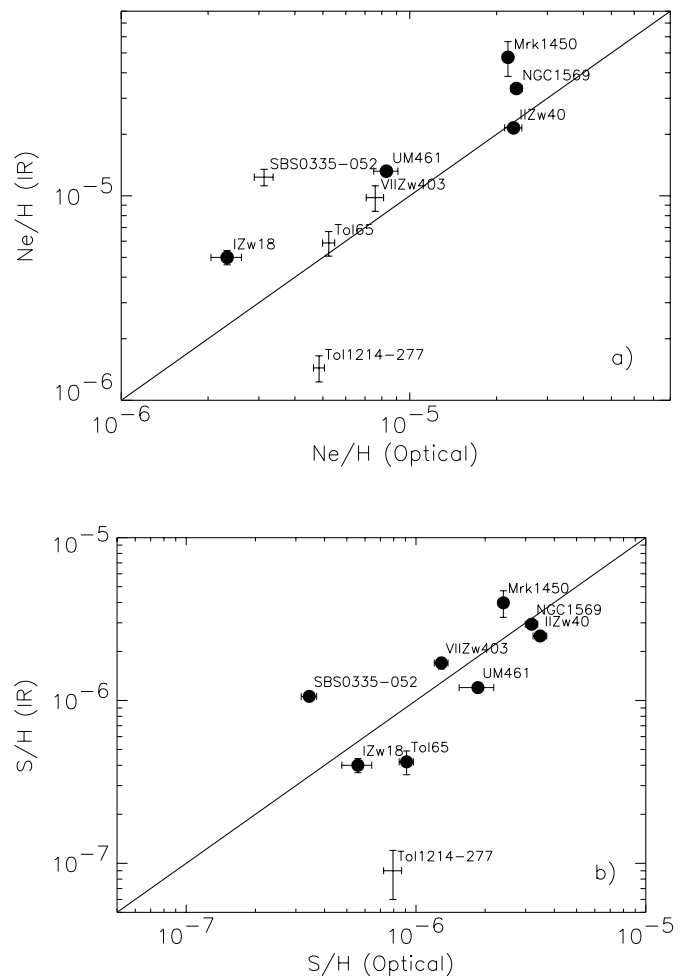

Fig. 5.—(a) Infrared-derived Ne/H as a function of the optical Ne/H abundances. The sources shown with only the error bars are those where [Ne II] or [S III] is not detected. The solid line represents the 1:1 line for the optically and infrared-derived abundances. (b) Same as (a), but for S/H (optical) vs. S/H (infrared) abundances.

measurement, a direct measure of the Hβ flux, and reddening derived from the same data. Our infrared results are less sensitive to the electron temperature, but affected by the uncertainty in the Hβ flux if the Huα line is not detected, and the uncertainty could be as large as 25%. In Figure 5a we plot the optically derived Ne/H against the infrared Ne/H. The solid line is the 1:1 proportion line for the infrared- and optically derived abundances, and we find that most of the sources are located above this line. A possible explanation for the higher infrared-derived neon abundances could be the presence of dust enshrouded regions which might have higher heavy-element abundances. This could explain the higher infrared metallicity found in SBS 0335−052E, but if this were true for the whole sample, it should also apply to the sulfur abundances. However, when we plot the S/H (optical) against the S/H (infrared) in Figure 5b, we find that the sources are located on both sides of the 1:1 proportion line. Alternatively, this could be due to the difference in the determination of element abundance using the infrared and optical methods. Because only Ne III is detected in the optical regime, the total elemental abundance of neon from the optical study is heavily dependent on the adopted ICF. In the infrared the [Ne II] line is detected in most of our sources, and we do not use any ICF for our study. Thus, the higher neon abundances derived from the infrared data compared to the optical results could also be due to the large uncertainty in the ICF used in the optical studies. Another possibility is that the temperature of the Ne III ion is lower than that of the O III ion as

found in some PNe (Bernard-Salas et al. 2002). Because the optical studies are based on T_e(O III) when calculating the ionic abundance of Ne III, that could also result in an underestimate of its abundance.

Finally, we explore the variation in the ratio of Ne/S as derived from the infrared and the optical data, and plot them as a function of O/H in Figure 6. Interestingly, we find that, with the exception of VII Zw 403, in all BCDs the infrared-derived Ne/S ratios are higher than the corresponding optical values. Izotov & Thuan (1999) indicate an average Ne/S ratio of 6.9 for the 54 supergiant H II regions they study in 50 BCDs using optical spectroscopy. The average of the optically derived Ne/S ratio for the nine sources in our sample is 6.5 ± 1.8, while the corresponding ratio from the infrared data is 11.4 ± 2.9, statistically higher than the optical results. As we mentioned earlier, no S II abundances could be determined with the *Spitzer* IRS data. However, in high-excitation objects such as BCDs, S II does not contribute much (∼10%) to the total elemental abundance; thus, it could not account for the factor of 2 difference in the ratio of Ne/S. Furthermore, such a discrepancy is not a result of metallicity, because we see no correlation in the dispersion between the infrared- and optically derived ratios of Ne/S with respect to O/H. If we divide the sources into a high-excitation group with sources that have a detectable [O IV] $\lambda 25.89$ μm line and a low-excitation group with
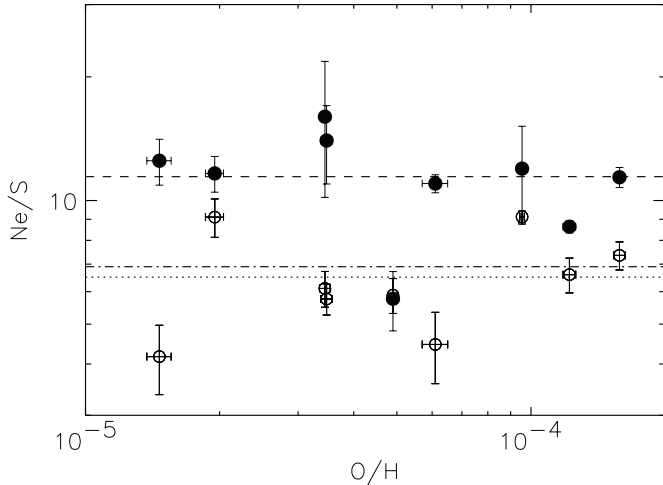
Fig. 6.—Abundance ratio of Ne/S as a function of O/H. The infrared-derived Ne/S ratios are indicated by the filled circles while the optically derived Ne/S ratios are shown by the open circles. The dashed line is the average Ne/S ratio from the infrared-derived elemental abundances, while the dotted line is average Ne/S ratio from the optically derived elemental abundances. The dash-dotted line represents the average Ne/S ratio from Izotov & Thuan (1999).

sources without any detection of [O IV], we still see no clear trend. Thus, the ionization field cannot explain the difference in the Ne/S ratios either. Moreover, no correlation is found between the Ne/S ratio and the extinction to the source. Even though the largest uncertainty in the infrared-derived abundances comes from the uncertainty in the Hβ flux in cases where no Huα is detected, when calculating the ratio of Ne/S, the Hβ flux cancels out; thus, our infrared-determined values for Ne/S should be fairly reliable. One possibility for the observed discrepancy could be that the difference in the infrared and optical results is again due to the ICF adopted in the optical studies.

5. METALLICITIES AND PAHs

The observed suppression of PAH emission in a low-metallicity environment is still an open topic (Madden 2000; Madden et al. 2006; Engelbracht et al. 2005; Wu et al. 2006; O'Halloran et al. 2006). One explanation on the absence of PAHs is that there is not enough carbon to form into PAH molecules in such metal-

poor environments, while an alternative possibility could be that the strong ionization field in low-metallicity environments may destroy the fragile PAH rings.

Previous studies relating the PAHs and metallicity were all based on the oxygen abundance measured from the optical, which could be associated with regions that are different from the ones where PAH emission originates. Because we have obtained the infrared measured neon and sulfur abundances, it is particularly interesting to compare the PAH strength with our metallicity estimates. Several BCDs in our sample do show PAH emission features, and an analysis of the PAH properties of our sample based on IRS low-resolution spectra was presented in Wu et al. (2006). We have obtained deeper spectra for some of the sources, so for consistency we have remeasured all features in our sample, and the results are given in Table 5. None of the sources with metallicity lower than ∼0.12 $Z_\odot$ show any detectable PAHs. For the sources where PAHs were detected, we calculate the equivalent widths (EWs) of the 6.2, 7.7, 8.6, and 11.2 μm features and find that the correlation between the PAH EWs and the metallicity is weak. This is not unexpected, because as discussed in Wu et al. (2006) the strength of PAHs in low-metallicity environments is a combination of formation and destruction effects. As a result, the dependency of PAH strength on the metallicity alone could have a substantial scatter.

6. CONCLUSIONS

We have studied the neon and sulfur abundances of 13 BCDs using *Spitzer* IRS high-resolution spectroscopy. Our analysis was based on the fine-structure lines and the hydrogen recombination line detected in the SH spectra of the IRS, combined with the radio continuum, Hα images, and integrated optical spectral data in some cases. We find a positive correlation between the neon and sulfur abundances, although sulfur appears to be more underabundant than neon (with respect to solar). The ratio of Ne/S for our sources is on average 12.5 ± 3.1, which is consistent with what has been found in other H II regions using infrared data. However, this average ratio appears to be higher than the corresponding optical value of 6.5 ± 1.8 (in nine BCDs), which could be due to the adopted ICFs in the optical studies. When comparing the newly derived neon and sulfur abundances with the oxygen abundances measured from the optical lines, we find a good overall agreement. This indicates that there are few completely

TABLE 5
PAH Measurements of the Sample

Object Name	PAH EW (μm)				Integrated Flux ($\times 10^{-14}$ ergs cm^{-2} s^{-1})			
	6.2 μm	7.7 μm	8.6 μm	11.2 μm	6.2 μm	7.7 μm	8.6 μm	11.2 μm
Haro 11	0.120 ± 0.003	0.227 ± 0.005	0.042 ± 0.003	0.099 ± 0.002	78.3 ± 1.8	180 ± 4	25.4 ± 1.6	67.2 ± 1.3
NGC 1140	0.479 ± 0.033	0.568 ± 0.024	0.091 ± 0.006	0.525 ± 0.032	42.1 ± 1.4	78.3 ± 1.8	11.1 ± 0.7	50.2 ± 2.5
SBS 0335−052E	<0.035	...	...	<0.015	<1.7	...	...	<1.0
NGC 1569	0.232 ± 0.013	0.380 ± 0.019	0.007 ± 0.005	0.129 ± 0.008	50.4 ± 2.4	118 ± 6	2.7 ± 1.6	68.1 ± 4.3
II Zw 40	0.044 ± 0.007	0.044 ± 0.006	0.006 ± 0.005	0.033 ± 0.006	13.2 ± 2.1	19.0 ± 2.8	2.8 ± 1.2	21.1 ± 3.7
UGC 4274	0.423 ± 0.032	0.497 ± 0.049	0.105 ± 0.012	0.495 ± 0.021	23.2 ± 1.2	43.3 ± 2.3	7.7 ± 0.9	29.1 ± 0.9
I Zw 18	<0.233	...	...	<0.116	<0.4	...	...	<0.1
Mrk 1450	0.207 ± 0.045	0.337 ± 0.143	0.084 ± 0.020	0.112 ± 0.017	1.8 ± 0.4	2.8 ± 0.9	0.7 ± 0.2	1.6 ± 0.2
UM 461	<0.663	...	...	<0.134	<1.5	...	...	<1.6
Mrk 1499	0.408 ± 0.040	0.526 ± 0.016	0.156 ± 0.011	0.721 ± 0.035	5.5 ± 0.3	10.9 ± 0.3	2.3 ± 0.2	7.3 ± 0.2

Notes.—Contrary to Wu et al. (2006), the wavelengths which we have chosen to determine the underlying continuum are fixed in the above measurements, which explains the minor discrepancies between these two studies. The symbol "..." indicates that no PAH EW measurement was possible, and this is mostly due to the low S/N of the corresponding spectrum. In this case, the determination of the continuum is highly uncertain and could significantly affect the value of the PAH EW. For SBS 0335−052E, the S/N is high enough, but no PAH features can be identified in its mid-infrared spectrum. We do not derive upper limits for the PAH EWs at 7.7 and 8.6 μm, because no reliable templates for those features are available.

dust-enshrouded H II regions in our BCDs, or if such H II regions are present, they have similar metallicities to the ones probed in the optical. Finally, the infrared-derived neon and sulfur abundances also correlate, with some scatter, with the corresponding elemental abundances derived from the optical data.

REFERENCES

Allende Prieto, C., Lambert, D. L., & Asplund, M. 2001, ApJ, 556, L63
Aloisi, A., Savaglio, S., Heckman, T. M., Hoopes, C. G., Leitherer, C., & Sembach, K. R. 2003, ApJ, 595, 760
Aloisi, A., et al. 2007, in IAU Symp. 241, Stellar Populations as Building Blocks of Galaxies, ed. A. Vazdekis & R. F. Peletier (Cambridge: Cambridge Univ. Press), 310
Anders, E., & Grevesse, N. 1989, Geochim. Cosmochim. Acta, 53, 197
Asplund, M., Grevesse, N., & Sauval, A. J. 2005, in ASP Conf. Ser. 336, Cosmic Abundances as Records of Stellar Evolution and Nucleosynthesis, ed. T. G. Barnes III & F. N. Bash (San Francisco: ASP), 25
Bergvall, N., & Oumlstlin, G. 2002, A&A, 390, 891
Bernard-Salas, J., Pottasch, S. R., Beintema, D. A., & Wesselius, P. R. 2001, A&A, 367, 949
Bernard-Salas, J., Pottasch, S. R., Feibelman, W. A., & Wesselius, P. R. 2002, A&A, 387, 301
Bernard-Salas, J., et al. 2008, ApJ, 672, 274
Cannon, J. M., Walter, F., Skillman, E. D., & van Zee, L. 2005, ApJ, 621, L21
Cohen, M., Megeath, S. T., Hammersley, P. L., Martín-Luis, F., & Stauffer, J. 2003, AJ, 125, 2645
Denicoló, G., Terlevich, R., & Terlevich, E. 2002, MNRAS, 330, 69
Draine, B. T. 2003, ARA&A, 41, 241
Engelbracht, C. W., Gordon, K. D., Rieke, G. H., Werner, M. W., Dale, D. A., & Latter, W. B. 2005, ApJ, 628, L29
Feldman, U., & Widing, K. G. 2003, Space Sci. Rev., 107, 665
Fluks, M. A., Plez, B., The, P. S., de Winter, D., Westerlund, B. E., & Steenman, H. C. 1994, A&AS, 105, 311
Gil de Paz, A., Madore, B. F., & Pevunova, O. 2003, ApJS, 147, 29
Grevesse, N., & Sauval, A. J. 1998, Space Sci. Rev., 85, 161
Guseva, N. G., Izotov, Y. I., & Thuan, T. X. 2000, ApJ, 531, 776
Henry, R. B. C., Kwitter, K. B., & Balick, B. 2004, AJ, 127, 2284
Higdon, S. J. U., et al. 2004, PASP, 116, 975
Ho, L. C., Filippenko, A. V., & Sargent, W. L. W. 1997, ApJS, 112, 315
Hogg, D. W., Tremonti, C. A., Blanton, M. R., Finkbeiner, D. P., Padmanabhan, N., Quintero, A. D., Schlegel, D. J., & Wherry, N. 2005, ApJ, 624, 162
Houck, J. R., Shure, M. A., Gull, G. E., & Herter, T. 1984, ApJ, 287, L11
Houck, J. R., et al. 2004a, ApJS, 154, 18
———. 2004b, ApJS, 154, 211
Hummer, D. G., Berrington, K. A., Eissner, W., Pradhan, A. K., Saraph, H. E., & Tully, J. A. 1993, A&A, 279, 298
Hummer, D. G., & Storey, P. J. 1987, MNRAS, 224, 801
Hunt, L., Bianchi, S., & Maiolino, R. 2005, A&A, 434, 849
Hunt, L. K., Dyer, K. K., Thuan, T. X., & Ulvestad, J. S. 2004, ApJ, 606, 853
Hunt, L. K., Thuan, T. X., Sauvage, M., & Izotov, Y. I. 2006, ApJ, 653, 222
Hunter, D. A., & Hoffman, L. 1999, AJ, 117, 2789
Izotov, Y. I., Chaffee, F. H., Foltz, C. B., Green, R. F., Guseva, N. G., & Thuan, T. X. 1999, ApJ, 527, 757
Izotov, Y. I., Chaffee, F. H., & Green, R. F. 2001, ApJ, 562, 727
Izotov, Y. I., Papaderos, P., Guseva, N. G., Fricke, K. J., & Thuan, T. X. 2004, A&A, 421, 539
Izotov, Y. I., Schaerer, D., Blecha, A., Royer, F., Guseva, N. G., & North, P. 2006, A&A, 459, 71
Izotov, Y. I., & Thuan, T. X. 1998, ApJ, 500, 188
———. 1999, ApJ, 511, 639
Izotov, Y. I., Thuan, T. X., & Guseva, N. G. 2005, ApJ, 632, 210
Izotov, Y. I., Thuan, T. X., & Lipovetsky, V. A. 1994, ApJ, 435, 647
———. 1997, ApJS, 108, 1
Kirshner, R. P., Oemler, A., Jr., Schechter, P. L., & Shectman, S. A. 1981, ApJ, 248, L57
Kniazev, A. Y., Grebel, E. K., Hao, L., Strauss, M. A., Brinkmann, J., & Fukugita, M. 2003, ApJ, 593, L73
Kobulnicky, H. A., & Skillman, E. D. 1997, ApJ, 489, 636
Kong, X., Cheng, F. Z., Weiss, A., & Charlot, S. 2002, A&A, 396, 503
Kunth, D., & Östlin, G. 2000, A&A Rev., 10, 1
Kunth, D., & Sargent, W. L. W. 1986, ApJ, 300, 496
Lebouteiller, V., Kunth, D., Lequeux, J., Lecavelier des Etangs, A., Désert, J.-M., Hébrard, G., & Vidal-Madjar, A. 2004, A&A, 415, 55
Loose, H.-H., & Thuan, T. X. 1985, in Star-Forming Dwarf Galaxies and Related Objects, ed. D. Kunth, T. Xuan Thuan, & J. Tran Thanh Van (Gif-sur-Yvette: Editions Frontieres), 73
Madden, S. C. 2000, NewA Rev., 44, 249
Madden, S. C., Galliano, F., Jones, A. P., & Sauvage, M. 2006, A&A, 446, 877
Marigo, P., Bernard-Salas, J., Pottasch, S. R., Tielens, A. G. G. M., & Wesselius, P. R. 2003, A&A, 409, 619
Martín-Hernández, N. L., Schaerer, D., Peeters, E., Tielens, A. G. G. M., & Sauvage, M. 2006, A&A, 455, 853
Martín-Hernández, N. L., et al. 2002, A&A, 381, 606
Melbourne, J., & Salzer, J. J. 2002, AJ, 123, 2302
Moustakas, J., & Kennicutt, R. C., Jr. 2006, ApJS, 164, 81
O'Halloran, B., Satyapal, S., & Dudik, R. P. 2006, ApJ, 641, 795
Osterbrock, D. E. 1989, Astrophysics of Gaseous Nebulae and Active Galactic Nuclei (Mill Valley: University Science Books)
Plante, S., & Sauvage, M. 2002, AJ, 124, 1995
Popescu, C. C., & Hopp, U. 2000, A&AS, 142, 247
Pottasch, S. R., & Bernard-Salas, J. 2006, A&A, 457, 189
Pustilnik, S. A., et al. 2005, A&A, 442, 109
Rosenberg, J. L., Ashby, M. L. N., Salzer, J. J., & Huang, J.-S. 2006, ApJ, 636, 742
Rubin, R. H., et al. 2006, in IAU Symp. 235, Galaxy Evolution Across the Hubble Time, ed. F. Combes & J. Palous (Cambridge: Cambridge Univ. Press), in press
———. 2007, MNRAS, 377, 1407
Salzer, J. J., Jangren, A., Gronwall, C., Werk, J. K., Chomiuk, L. B., Caperton, K. A., Melbourne, J., & McKinstry, K. 2005, AJ, 130, 2584
Searle, L., & Sargent, W. L. W. 1972, ApJ, 173, 25
Shi, F., Kong, X., Li, C., & Cheng, F. Z. 2005, A&A, 437, 849
Simpson, J. P., & Rubin, R. H. 1990, ApJ, 354, 165
Simpson, J. P., Rubin, R. H., Colgan, S. W. J., Erickson, E. F., & Haas, M. R. 2004, ApJ, 611, 338
Skillman, E. D., Kennicutt, R. C., & Hodge, P. W. 1989, ApJ, 347, 875
Spoon, H. W. W., Marshall, J. A., Houck, J. R., Elitzur, M., Hao, L., Armus, L., Brandl, B. R., & Charmandaris, V. 2007, ApJ, 654, L49
Stasińska, G. 2007, in The Emission-Line Universe, ed. J. Cepa and F. Sanchez (Cambridge: Cambridge Univ. Press), in press (arXiv: 0704.0348)
Thuan, T. X., Hibbard, J. E., & Lévrier, F. 2004, AJ, 128, 617
Thuan, T. X., Izotov, Y. I., & Lipovetsky, V. A. 1995, ApJ, 445, 108
Thuan, T. X., Lecavelier des Etangs, A., & Izotov, Y. I. 2002, ApJ, 565, 941
Thuan, T. X., Sauvage, M., & Madden, S. 1999, ApJ, 516, 783
Tsamis, Y. G., & Péquignot, D. 2005, MNRAS, 364, 687
Verma, A., Lutz, D., Sturm, E., Sternberg, A., Genzel, R., & Vacca, W. 2003, A&A, 403, 829
Vermeij, R., & van der Hulst, J. M. 2002, A&A, 391, 1081
Vilchez, J. M., & Pagel, B. E. J. 1988, MNRAS, 231, 257
Werner, M., et al. 2004, ApJS, 154, 1
Wu, Y., Charmandaris, V., Hao, L., Brandl, B. R., Bernard-Salas, J., Spoon, H. W. W., & Houck, J. R. 2006, ApJ, 639, 157
Wu, Y., et al. 2007, ApJ, 662, 952
Zwicky, F. 1966, ApJ, 143, 192